Journal of Colloid and Interface Science 354 (2011) 386–395

Contents lists available at ScienceDirect

Journal of Colloid and Interface Science

www.elsevier.com/locate/jcis

Simulations of novel nanostructures formed by capillary effects in lithography

Jiansheng Feng [a], Jonathan P. Rothstein [b,*]

[a] Physics Department, University of Massachusetts, Amherst, United States
[b] Department of Mechanical and Industrial Engineering, University of Massachusetts, Amherst, United States

ARTICLE INFO

Article history:
Received 28 July 2010
Accepted 15 October 2010
Available online 11 November 2010

Keywords:
Capillary Force Lithography
Three-dimensional meniscus
Contact angle
Corner rounding
Star-shaped capillary

ABSTRACT

High aspect ratio three-dimensional nanostructures are of tremendous interest to a wide range of fields such as photonics, plasmonics, fluid mechanics, and biology. Recent developments in capillary force lithography (CFL) have focused on taking advantage of the formation of menisci to enhance the functionality of small size-scale structures. In this study, simulations of the three-dimensional shapes of equilibrium menisci formed in capillaries with various cross-section geometries are studied. The capillary cross sections include regular polygons and equilateral star-shapes with sharp and rounded corners. The characteristic dimension of the physical lithography systems which are simulated is on the order of 100 nm. At such size-scale, surface-tension-effects are predominant, and as a consequence, our simulations demonstrate that nanometer-sized structures with great application potentials can be fabricated. Specifically, this study demonstrates that surfaces with three-dimensional nanoscale structures can be fabricated from templates with micron or sub-micron features through the development of cusps in the corners of the polygonal capillaries. Quantitatively, the effects of contact angle, corner angle, meniscus confinement, and corner rounding radius are examined and scaling analyses are presented to describe the dependencies of the height variation across the meniscus on these parameters. These simulations serve as useful guides for extending the development and implementation of capillary force lithography.

1. Introduction

As the limit of imprint lithography is pushed to smaller length scales, a great deal of research effort has focused on utilizing capillary forces to the advantage of lithography techniques. Capillary force, as one of the predominant forces at the nanometer size-scale, can be used not only to expedite micro- and nano-scale imprint lithography, but also to enable the formation of interesting and useful features on the lithographic products with details finer than those of the original molds [1–8]. These techniques take advantage of interfacial tension and wettability to control both the rate and the extent of the rising capillary and the resulting meniscus curvature. For example, Bruinink et al. [3,4] have reported a technique of using the edge of a meniscus formed by capillary force lithography (CFL) as a mold of making second-generation stamps with increased resolution. Moreover, it has also been shown in CFL experiments that ring-like structures can be made taking advantage of the height variations of menisci formed in cylindrical capillaries [5,6]. However, it should be noted that only linear or ring-like structures have been reported to date; few experimental results have been reported with different cross-sectional geometries, even as simple as triangles or rectangles.

In this work, we extend previous research in this area to exploit other interesting and potentially useful structures that can be created by capillary forces at the nanoscale. Of particular interest, is the formation of unique structures resulting from the confinement of the meniscus by capillaries with polygonal and star-shaped cross sections as seen in Fig. 1a. It has been shown for low-gravity fluid systems that crown-like menisci, as seen in Fig. 1b, should be expected in capillaries with polygonal cross sections if the wetting conditions are properly chosen [9–11]. These studies, which addressed a very different set of problems, i.e., liquid fuel storage in the weightlessness of space flight, are an excellent starting point and proof-of-concept for the work presented here. However, their focus was primarily the existence criteria for dichotomous behavior of the meniscus and the meniscus shape and height were not fully quantified.

There is a relatively small number of papers addressing the issues specific to the three-dimensional shape of capillary surfaces in complex, non-circular, geometries [9–14]. Additionally, it is important to note that none of these papers specifically addressed CFL or the issues specific to CFL. In these studies, the contact line was sometimes neglected [12]. Even when proper boundary conditions were applied, the height variation was usually not specified [9–11,14], or the geometry was simply too general [13]. For CFL,

* Corresponding author. Address: 160 Governors Drive, 219 ELab MIE Department, University of Massachusetts, Amherst, MA 01003, United States, Gunness Lab 16 (Office). Fax: +1 413 545 1027.
E-mail address: rothstein@ecs.umass.edu (J.P. Rothstein).

0021-9797/$ - see front matter © 2010 Elsevier Inc. All rights reserved.
doi:10.1016/j.jcis.2010.10.030

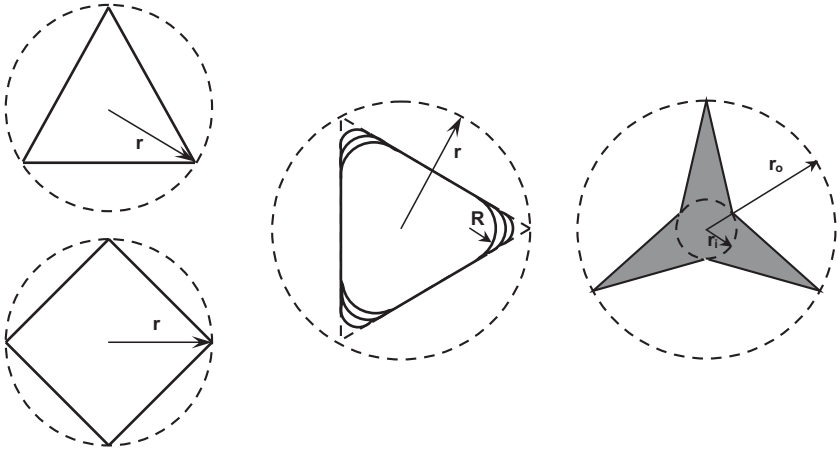

Fig. 1a. Schematic diagrams of cross-sectional geometries: (left) regular triangle and rectangle, with radius of circumscribed circle r; (middle) rounded corner triangle with various corner rounding radius R; (right) three-armed star with sharp corners, the convex corners of which all lie on the circumscribed circle with radius r_o, while the concave corners all lie on the inscribed circle with radius r_i. Additional note for star-shapes: the convex corners can also be rounded just like those of the triangle (figure not shown here).

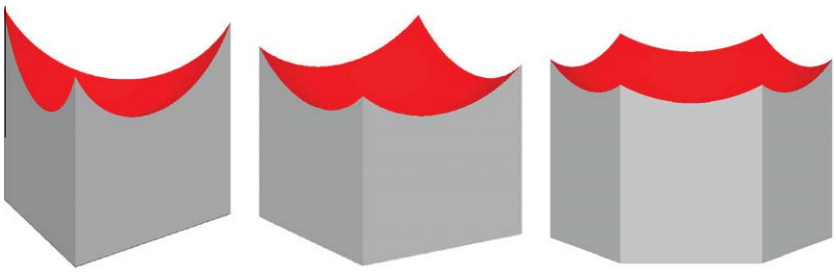

Fig. 1b. Schematic diagrams of menisci formed in capillaries with polygonal cross sections.

it is of great importance to specifically focus on the height variation of the meniscus because that dictates the additional functionality associated with the third dimension, specifically, the contrast of anisotropic etching if the resulting structures are to eventually be used as an etching mask. The geometries and wetting properties implemented in our simulations were chosen to investigate a number of important practical aspects of CFL, including the impact of rounding the corners of the polygons. In our study, numerical simulations were used to minimize the surface energy and calculate the position of the contact line and the shape of menisci at equilibrium. The important factors that govern the geometric characteristics of the resulting structures were investigated. These parameters included contact angle, surface tension, number of sides of the polygon or star as well as the radius of curvature and angle of the polygonal corners. We will show that smaller contact angles, cross sections with smaller internal angles or smaller corner rounding lead to taller cusps on the crown-like-menisci. Our results present the dependence of the height of those cusps on contact angle and cross-sectional geometry. Finally, we will show that star-shaped capillaries can be used to produce super-fine, high aspect ratio, three-dimensional hierarchical structures in capillary force lithography. It is worth mentioning that, in CFL a viscous liquid (e.g., polymer melt) is typically used instead of a Newtonian liquid. Also, the hydrostatic pressure inside the cavity is changing with time [15]. These factors play critical roles in the kinetics of the fluids. In our study, however, since we are mostly interested in the thermodynamic equilibriums, these factors do not affect the results. Specifically, the non-Newtonian nature of the fluids might affect the growth process due to their viscoelasticity the variation of their viscosity as response to shear, but that does not change the equilibrium states. The hydrostatic pressure inside the cavity is always isotropic, which means that it could only affect the height of the fluid column but not the shape of the meniscus.

2. Simulation

2.1. Simulation setup

Surface Evolver was used to simulate the equilibrium state of a fluid body inside a capillary. The Surface Evolver is an open-source computer program which uses a gradient descent method to minimize the energy of a surface subject to constraints [16]. Initially, a bulk of fluid is defined with a fixed volume bounded by a set of vertical planar constraints which represent the side walls (with no penetration) of the capillary and a horizontal planar constraint at the bottom (to represent permanent attachment on the substrate). This simulation technique cannot be used to simulate the dynamics of capillary rise. However, this model will give the correct result for the equilibrium state of the meniscus because the equilibrium state is path independent.

To study the evolution of the equilibrium meniscus in capillary force lithography, two categories of cross-sectional geometries were simulated – polygons and stars. In each category, geometries with both sharp corners and rounded corners with a broad range of radii of curvature were studied. Regular convex polygonal cross sections were centered at the origin and circumscribed by a circle corresponding to a radius of physical dimension $r = 100$ nm. Polygonal cross sections with rounded corners are created by trimming the corners of the regular polygons into circular arcs with radii of curvature from $R = 0.1r$ to $R = 0.3r$. Each of these round arcs is tangent to both sides of the corner in which it is placed, as seen

in Fig. 1a. To facilitate comparisons between different geometries, all rounded polygons with the same symmetry order share the same regular polygonal frame. Similarly for star geometries, the radius of circumscribed circle is fixed to be r_o = 100 nm, while the radius of inscribed circle (on which all the concave corner vertices lie), r_i, varies between 20 nm and 50 nm. This is shown schematically in Fig. 1a. The same manipulations are carried out in order to generate star geometries with rounded corners as described previously for polygonal geometries.

After a cross-sectional geometry is generated, it is defined to the Surface Evolver as a set of planar constraints which are applied to x and y and apply for all values of z. Vertices on the constraint planes are bounded on the plane at all time (but are allowed to move along the plane). The tube defined by these constraints is then filled with a column of fluid with an initial height equal to the circumscribing radius. As an initial state, the top and bottom surfaces of the fluid column are both flat and horizontal. During an evolution, all the side surfaces of this fluid column are in intimate and permanent contact with the walls of the tube, and its bottom surface is permanently bounded on the plane constraint $z = 0$. The top surface is free to adopt any shape that minimize the total energy of the system consists of both the fluid body and the capillary tube.

2.2. Size effect and contact angle

Typically, surface forces scale with the length of the contact line and therefore the first power of the characteristic length, which in our case is the radius of the circumscribed circle. Conversely, body forces scale with the volume and therefore as the third power of the characteristic length. As a result, the smaller the length, the more dominant the surface forces become. For this reason, surface forces play an important role in material behaviors at small size-scales while gravitational effects can be neglected [17]. In this study, the characteristic length scales of the fluid systems are set between 100 nm and 1 μm. Since the algorithm used by the Surface Evolver is unit independent, the size effects are translated into the value of the gravitational constant. By using a unit analysis based on comparing the gravitational force and the surface tension, it is calculated that the effective gravitational constant for our characteristic length scale is essentially zero.

In this discussion, only the partial wetting regime is considered, where the contact angle between the fluid and the side walls of the capillary is $\theta < 90°$. The contact angle, θ, always refers to the (equilibrium) material contact angle defined by the Young equation $\gamma_{SG} = \gamma_{SL} + \gamma_{LG}\cos\theta$ [18]. Here γ_{SG} is the interfacial tension between the solid and gas phases, γ_{SL} is the interfacial tension between the solid and liquid phases, and γ_{LG} is the interfacial tension between the liquid and gas phases. The side walls of capillary are always assumed to be smooth, homogenous, and rigid. Additionally, no hysteresis of contact angle is considered, although in the corresponding experiments the results will likely be dependent on the advancing contact angle because it is a capillary filling process. Under those assumptions, contact angle can be determined as a function of interfacial energies by $\cos\theta = (\gamma_{SG} - \gamma_{SL})/\gamma_{LG}$. Physically, for every unit area growth of the side surfaces of the fluid column, a unit area of solid–gas interface is replaced by a unit area of solid liquid interface and resulting in a total change of energy of the system of $\gamma_{SL} - \gamma_{SG}$.

For every cross-sectional geometry there exists a critical contact angle due to Rayleigh–Taylor interfacial instability [10,11,14]. Under partial wetting condition, if the contact angle between the fluid and the wall of the capillary is larger than or equal to that critical value, the equilibrium extent of the meniscus growth along the length of the capillary is finite. However, if the contact angle is smaller than this critical value, the equilibrium meniscus can become infinitely long. Finn et al. [11,14] have shown through a rigorous mathematic analysis that at a sharp corner the critical contact angle is $\theta_c = \pi/2 - \alpha$, where α is half of the internal angle of the corner.

2.3. Evolution and equilibrium criteria

Once the geometry was defined, Surface Evolver was used to determine the equilibrium shape of the meniscus. Each simulation consisted of three stages – initiating, approaching, and stabilizing – to gain faster convergence. In the initiating stage, three refinements to each edge with length greater than $0.05r$ (or $0.05r_o$ in the star geometry cases) were performed. Each refinement was done by putting a vertex at the midpoint of a targeted edge so that it could be split into two edges each with half the length of the initial one. At this stage, as many steps as needed were performed to bring the energy gradient down to less than 1.0×10^{-6} (in simulation unit assumed by Surface Evolver) per 10 steps. In the approaching stage, conjugate gradient mode is toggled, and another three refinements were performed. At this stage the energy gradient was brought down to less than 1.0×10^{-8} per 10 steps. The simulations were continued to the stabilizing stage, where as many refinements and evolutions as needed were performed to satisfy a set of equilibrium criteria, which will be described in detail below. The extent and shape of the final, equilibrium meniscus was extracted and analyzed to understand the trends.

With respect to Capillary Force Lithography, the quantity of most interest is the difference in elevation between the highest and the lowest points on a meniscus, which we will refer to as h from this point on. To match the sign of elevation with that of the cosine of the contact angle, a convention is used where concave menisci have positive elevations while convex menisci have negative elevations. Since the final state of the meniscus is usually a curved surface, and in Surface Evolver a curved surface is discretized into a union of flat triangular facets, the sizes of these facets, or grid resolution, can affect the final shape of the meniscus [13]. Finer grid resolutions give more accurate shapes but the simulations take a longer time to converge. Moreover, the change in energy with each step slows as the system approaches equilibrium. Thus a threshold of this energy gradient is needed to determine whether the system has reached equilibrium. A series of convergence tests were performed using the regular polygon geometries. Based on these test results, a set of criteria according to which equilibrium is determined are chosen as following: maximum length of a single edge less than 5.0 nm; minimum length of a single edge greater than 0.5 nm; equiangulation is completed; the change of energy (as evaluated by Surface Evolver) within the last ten steps is smaller than 1.0×10^{-10}. This set of equilibrium criteria corresponds to a less than 1% change in the value of elevation in all the geometries and contact angle values that have been studied. Since the maximum elevation we have observed is on the order of 100 nm, one percent of the elevation corresponding to actual physical dimension less then 1.0 nm. When plotted at a log–log scale to find the characteristic power index, this error has no measurable effect on the results. The dependence of elevation on the other parameters studied produced variations in the meniscus height much larger than the 1.0 nm uncertainty due to resolution effects.

3. Results

The shape of meniscus formed in a cylindrical capillary is a classically studied problem [17]. There exists a characteristic length scale, known as the capillary length $L_{cap} = \sqrt{\gamma/\rho g}$, below which surface tension dominates over gravity and the meniscus formed inside the capillary adopts a shape very close to a portion of a sphere. For pure water at standard temperature and pressure, the

capillary length is about $L_{cap} \approx 2$ mm. Polymeric fluids typically have much lower surface tensions then water resulting in capillary lengths on the order of hundreds of microns. For a cylindrical capillary with a radius of $r = 100$ nm, it can be therefore assumed that the shape of the meniscus is a spherical cap. In this case the analytical solution for elevation, h, as a function of cross-sectional radius, r, and contact angle, θ, can be shown to be: $h = r(1 - \sqrt{1 - \cos^2\theta})/\cos\theta$. In the limit of $\cos\theta \to 0$, we get $h \to (r/2)\cos\theta$; at the limit of $\cos\theta \to 1$, we get $h \to r[1 - \sqrt{2(1 - \cos\theta)}]$. The predictions of the meniscus height from our simulation of cylindrical capillaries are superimposed over the analytical solution in Fig. 2 inset. The simulations match the theory very well over all the contact angles tested. Plotting h versus $\cos\theta$ in a log–log scale (Fig. 2), we can see that at small and medium $\cos\theta$ the slope mostly remains constant, which indicates a power law dependence of elevation over $\cos\theta$; at the regime where $\cos\theta$ is close to one, however, the slope increases very rapidly. The power index measure from the linear portion of the log–log plot is approximately 1.05 (the slope of the fit line varies slightly depending on the range of $\cos\theta$ over which fitting is performed).

For patterns of lines, the elevation of the meniscus due to the confinement of parallel walls can be easily calculated analytically: $h_L = (1 - \sin\theta)d/2$, where d is the spacing between the parallel walls. This, of course, is only an exact solution for an infinitely long straight line where the effects on the meniscus from the ends of the line can be neglected. If, however, we consider a straight line with finite length, the existence and shape of the line's endcap must be accounted for, as it will induce a secondary curvature along the length of the line. The majority of the meniscus located towards the midpoint of the line and away from the ends should remain two-dimensional. However, the exact the shape of the meniscus near the ends of the lines is more complicated and, as we will see in the case of regular polygons, is directly related to the details of the shape of the endcap (polygonal or circular), the contact angle between the fluid and the walls of the capillary and the curvature of any sharp corners.

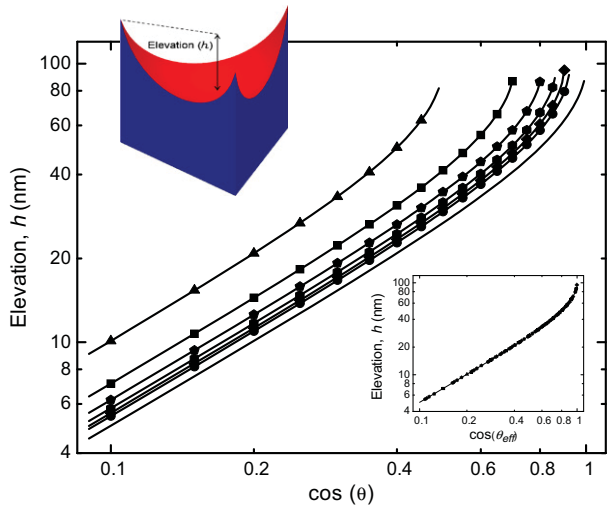

Fig. 2. Elevation of meniscus, h, as a function of contact angle, θ, for capillaries whose cross sections are regular polygons with sharp corners. Data points are from simulation. Cross-sectional geometries including: (▲) triangle, (■) square, (⬟) pentagon, (⬣) hexagon, (♦) heptagon, and (●) octagon. Also plotted are the analytical solutions of elevation resulted in regular polygonal and circular cross section as a function of contact angle (solid lines). The inset shows the elevation curves collapse onto a single line when plotted against cosine of effective contact angle; discrepancy for any one of those data points is less than 1%.

3.1. Sharp regular polygons

The shape of a capillary can have a large impact on the resulting meniscus shape and height. In this section, we investigate a series of capillaries with cross sections as regular polygons each of which is circumscribed by a circle with a radius of $r = 100$ nm. As before, gravity is negligible and the fluid partially wets the capillary. For these geometries it has been shown that these menisci are in fact sections of a sphere much like the cylindrical capillary if the material contact angle is not less than the critical contact angle [20,21]. A simple way to understand this solution is shown schematically in Fig. 3. Start with a vertical plane P intercepting a sphere S whose center is point O. Fix the distance, d, between plane P and point O, while allowing the radius, R_s, of sphere S to vary. When $R_s = d$, P is tangent to S, and the normal of P lines up with the local normal of S at the tangent point, i.e., intercepting angle $\beta = 0°$; when $R_s \to \infty$, the intercepting angle $\beta \to 90°$. For any particular value of R_s between d and ∞, the intercepting angle β is a constant at every point on the intercepting circle due to rotational symmetry about every horizontal line that go through point O. The value of β can be anywhere between 0° and 90°, and it is a function of R_s only. Since all the sides of a regular polygon have the same distance to its center, based on the argument above, a spherical meniscus (here, in fact, only the lower hemisphere is needed; the upper hemisphere corresponds to cases where contact angle is between 90° and 180°) can satisfy any specified contact angle at every point on the contact line on every side wall. Moreover, a sphere has constant mean curvature at every point, which satisfies the requirement of uniform Laplace pressure across the interface under zero-gravity condition.

Changing the cross-sectional geometry from a circle to a regular polygon is effectively only changing the radius of the spherical surface on which the meniscus lies. This in turn is physically consistent with changing the contact angle θ. For a regular polygon, it can be found that the new radius is $R_s = r\sin\alpha/\cos\theta$, where $\alpha = (n - 2)\pi/(2n)$ is half of the internal angle of a corner of an n-sided regular polygon. The elevation, or the height difference of the meniscus between the center and a corner of the capillary, is $h = r\sin\alpha[1 - \sqrt{1 - (\cos\theta/\sin\alpha)^2}]/\cos\theta$. In the limit that $n \to \infty$, the result for a circular cross section is obtained. Fig. 2 shows elevation as a function of contact angle calculated based on this analytical solution for cross-sectional geometries as triangle, rectangle, pentagon, and hexagon. It is immediately clear that if the available contact angles are limited to relatively close to 90°, which is usually the case for CFL due to the low surface tensions of PDMS and polymer melts, it is possible to take advantage of triangular geometry to achieve relatively high elevation differences across the meniscus.

If one defines an effective contact angle, θ_{eff}, such that $\cos\theta_{eff} = \cos\theta/\sin\alpha$, then all the data for the sharp regular polygons in Fig. 2 should collapse onto a single master curve. This is shown in the inset of Fig. 2 which plots h as a function of $\cos\theta_{eff}$. Physically, this effective contact angle θ_{eff} is the angle between the differential portion of the meniscus at the corner of the cross section and the side edge of the capillary. Notice that when $0° < \theta < 90°$, θ_{eff} is always less than θ. The instability of a meniscus formed in a polygonal capillary occurs at the corners first. As a result, the critical contact angle for a regular polygonal capillary is reduced to $\theta_c = \pi/n$, where n is the number of sides. Specific values of critical contact angle for regular polygons are listed in Table 1.

The equivalency between changing cross-sectional geometry and rescaling of the contact angle also implies that the upper limit of elevation of a stable meniscus is the radius of the circumscribed circle of the cross-sectional polygon, r, because that is the best of what a circular cross section can provide (with 0° contact angle

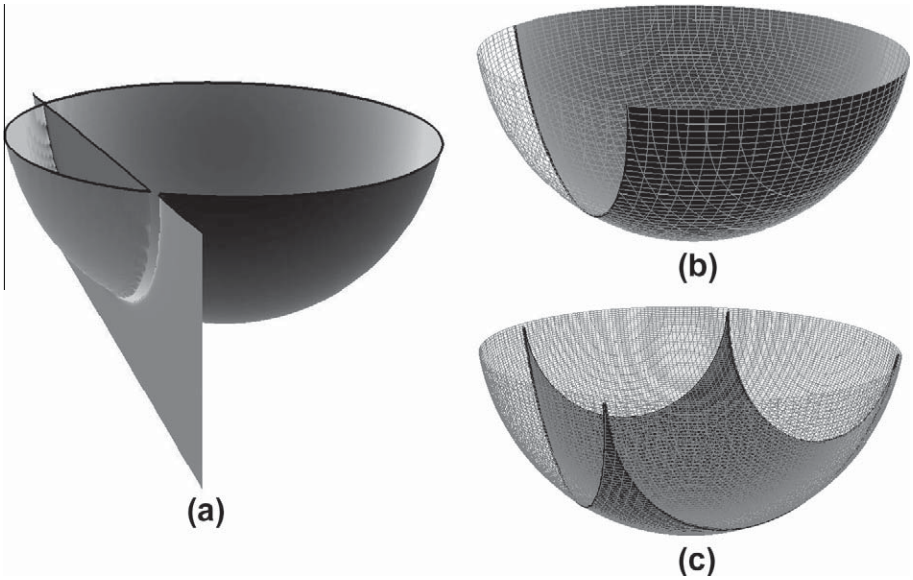

Fig. 3. Schematics of the construction of analytical solution. (a) a hemisphere intercepted by a plane; (b) the intercepting angle between the plane and the hemisphere is the same at every point due to rotational symmetry; (c) the meniscus formed in a rectangular capillary is part of a hemisphere.

Table 1
Reciprocal sine of half internal angles, critical contact angles and the cosine of critical contact angles for cross-sectional regular polygons with different orders of symmetry.

Geometry	Triangle	Rectangle	Pentagon	Hexagon	Heptagon	Octagon	Circle
$1/\sin(\alpha)$	2.0	1.4142	1.2361	1.1547	1.1099	1.0824	1.0
θ_c	60°	45°	36°	30°	25.7°	22.5°	0.0°
$\cos(\theta_c)$	0.5	0.7071	0.8090	0.8660	0.9010	0.9239	1.0

so that the meniscus is exactly the lower hemisphere). However, with a triangular cross section, for example, the stability limit can be approached with much larger contact angles and such heights cannot be achieved.

In order to understand the effect of wetability of the meniscus shape, simulations were performed for material contact angles in the range between θ_c and 90°. Fig. 2 plots the simulation results of the elevation of menisci formed in polygonal cross sections versus the cosine of material contact angles. All curves for regular polygonal cross sections follow the same trend, and when θ is converted into θ_{eff}, as shown in the inset, all those curves collapse on top of the curve for circular cross section. When the simulation results are compared with the analytical results, the discrepancy of any individual data point is below 1%, which demonstrates the reliability of the simulation procedure. Notice on the log–log plot, within the range where $\cos(\theta_{eff})$ from 0.1 up to 0.7, or equivalently θ_{eff} from 85° down to about 45°, the response of elevation to the change of $\cos(\theta_{eff})$ is fairly linear (the portion is fairly straight and the slope is close to 1.0), and this linear portion covers about 40% of the elevation range. For the other half of the effective contact angle range, from 45° to 0°, the height – contact angle behavior is highly non-linear. As a result, a relatively small reduction in θ_{eff} can result in a significant increase of elevation. As a side note, when the contact angle is between 90° and 180°, it is easy to prove based on symmetry that the equation $h = r[1 - \sqrt{1 - (\cos\theta_{eff})^2}]/\cos\theta_{eff}$ is still valid, only now the resulting elevation is negative because the meniscus lies on the upper hemisphere, or $h(\cos\theta) = -h(\cos(\pi - \theta))$ when $90° \leqslant \theta \leqslant 180°$. Practically, this means that if one chooses to use a low adhesion pair of fluid and solid for easier separation between the mold and the product after CFL, one needs to also realize that this choice may also hinder the filling of fluid into capillary especially in small dimensions and at sharp corners.

3.2. Rounded polygons

Experimentally, it is difficult to fabricate nanoscale capillaries with perfectly sharp corners. In fact, when doing CFL of nanoscale features, the corners of the structures on the mold are always rounded to some degree. To better guide the design of CFL experiments, a series of simulations were performed for geometries with regular polygonal cross sections and rounded corners. As a first approach the rounding of polygon corners was chosen to be circular and tangent to both sides of the included angle. The intuitive expectation is that the rounding of corners should reduce the elevation of the meniscus when compared to the same geometry with sharp corners and the same material contact angle. In addition, we expect rounding the corners will allow the meniscus to be stable over a larger range of contact angles because as the rounding radius increases the meniscus formed within the polygonal capillary should eventually approach that formed in a circular capillary.

The response of meniscus elevation to the change of contact angle is shown in Fig. 4a. The results for triangular cross sections with rounded corners with rounding radii of 10 nm, 20 nm, and 30 nm behave similarly with changing contact angle to those of regular polygons, showing an elevation decrease as the corner rounding is increased. All curves appear to be qualitatively similar, but shifted with respect to $\cos(\theta)$. One way to quantify the change in response is to determine the slopes of the linear portion of curves in Fig. 4a, which are listed in Table 2. Although they appear very similar at small values of $\cos(\theta)$, there are small differences in the functional dependence of $h \propto \cos(\theta)^n$. The power of the polynomial is

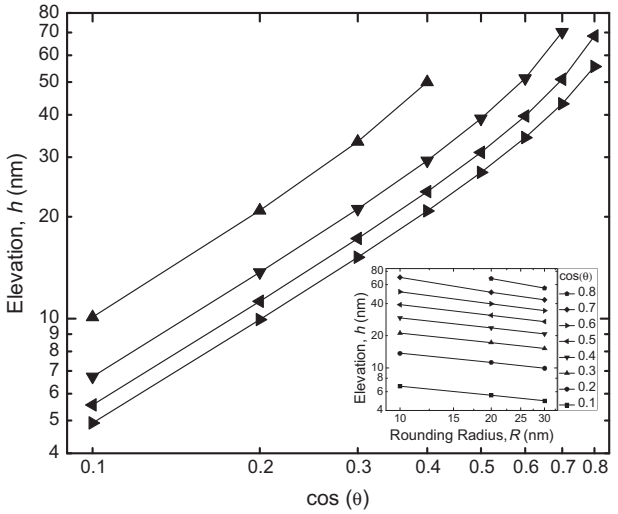

Fig. 4a. Elevation of meniscus, h, as a function of contact angle, θ, for capillaries whose cross sections are triangles with sharp and rounded corners. Data include: (▲) sharp triangle, triangles with radii of (▼) $R = 0.1$, (◀) $R = 0.2$, and (▶) $R = 0.3$. The inset at the bottom right shows elevation as a function of rounding radius, as $\cos(\theta)$ increases from 0.1 to 0.8 (from bottom to top), showing a linear dependency of the meniscus height on the rounding radius.

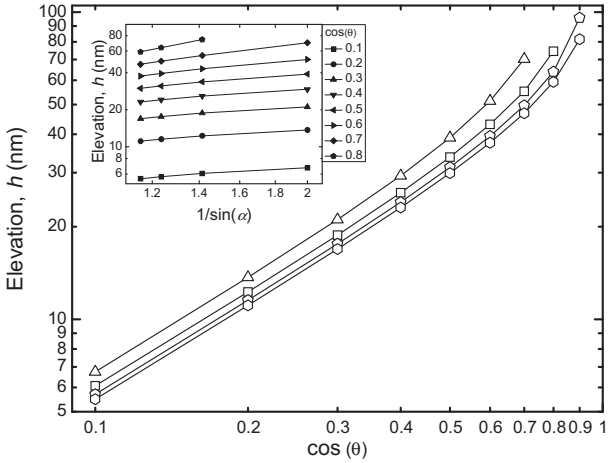

Fig. 4b. Elevation of meniscus, h, as a function of contact angle, θ, for capillaries whose cross sections are polygons with rounded corners (where $R = 0.1$ in all cases). Data include rounded: (△) triangles, (□) rectangle, (⬠) pentagon, and (⬡) hexagon. The inset at the top left shows elevation h as a function of $1/\sin(\alpha)$, as $\cos(\theta)$ increases from 0.1 at the bottom to 0.8 at the top.

found to decrease from $k = 1.08$ for the sharp case to $k = 1.04$ for the case where $R = 30$ nm. In particular, with increasing rounding radii curves shift to the right, but the shifting becomes slower when rounding radii get larger. These observations indicate that the effective contact angle increases with increasing rounding radius. If one instead looks at the elevation of the meniscus as a function of rounding radius, as shown in the inset of Fig. 4a, this shifting effect can be quantified. The characteristic length scale (the radius of circumscribed circle) is kept to be 100 nm, and the rounding radii are 10 nm, 20 nm, and 30 nm in the simulation results presented here. As seen in the inset of Fig. 4a, there are clear power-law dependences of elevation on rounding radius, which vary from −0.29 to −0.45 over the span of $\cos(\theta)$ values from 0.1 to 0.8. The specific values of the slope of Fig. 4a inset are listed in Table 5. It is worth emphasizing that the power law relations we present here are useful in understanding dependencies, however, they should not be extrapolated to the region where R (rounding radius) is significantly smaller than 10 nm because they lead to a singularity at $R = 0$, the case where corners are perfectly sharp.

For completeness, a series of simulations were performed for regular polygons with similar rounded corners cross-sectional geometries. In Fig. 4b, values of h as a function of $\cos(\theta)$ are presented for rounded triangle, rectangle, pentagon, and hexagon, all with a rounding radius equal to 10 nm at each corner. As expected, the elevation decreases in all cases in comparison to the same polygon with sharp corners shown in Fig. 2 and Table 3. As seen with triangles, the sharp and rounded data are qualitatively the same, just shifted to smaller heights. It is worth noticing that the reduction of elevation for rounded polygons is not only the result of the reduction of confinement due to corner rounding, but also due to the fact that rounded polygons have slightly smaller cross sectional area than the sharp corner ones as a result of the way they were created, see Fig. 1a. If there were only the dimension effect contributing to elevation decrease, one would expect that the menisci resulting from different rounding radii should entirely overlap on top of each other up to the point that the meniscus contacts the rounded corner. To investigate this hypothesis, the position of the contact lines in a series of triangular capillaries with various degrees of corner rounding and the menisci formed in them are shown in Fig. 5. As seen in Fig. 5, the effect of the rounded corner propagates far from the corner itself and changes the shape and nature of the meniscus well away from the corner. Thus it is clearly not simply an area effect.

Table 2
Slopes of the linear portion of the h versus $\cos(\theta)$ log–log curves for sharp and rounded triangular cross sections.

	Sharp	$R = 10$ nm	$R = 20$ nm	$R = 30$ nm
Slope, k	1.082	1.056	1.043	1.037

3.3. Sharp regular stars

Polygons, while interesting, are not the only shapes that are fabricated using CFL. If the goal is to maximize the height variation, an intriguing geometry is a regular star. In this section, we present a series of simulations to evaluate elevation of menisci formed inside capillaries with regular star cross sections. The arguments presented in Section 3.1 can be applied to regular star-shaped cross-sectional capillaries, because all the sides of a regular star also have the same distance to its center. Thus the menisci formed within a star can be described by a section of a sphere if gravity is neglected. The radius of the sphere on which the meniscus lies depends on r_i, r_o, n, and θ with the following relationship $R_s = r_o \sin(\pi/n)/[\cos\theta\sqrt{(r_o/r_i)^2 + 1 - 2(r_o/r_i)\cos(\pi/n)}]$, where r_o is the radius of the circumscribed circle of the cross-sectional star on which all the convex vertices lie and r_i is the radius of the inscribed circle of the cross-sectional star on which all the concave vertices lie, and n and θ are order of symmetry and material contact angle, respectively. The ratio r_o/r_i depicts the slenderness of the arms of the stars, and thus determines the internal angle of the concave vertices. Similar to polygon cases, smaller internal angle, or greater r_o/r_i ratio, gives smaller R_s. Additionally, if the contact angle geometry combination results in $R_s = r_o$ then it is at the critical contact angle $\cos\theta_c = \sin(\pi/n)/\sqrt{(r_o/r_i)^2 + 1 - 2(r_o/r_i)\cos(\pi/n)}$. Any contact angle, θ, smaller than this critical value θ_c will yield an elevation on the meniscus which can be calculated by the equation $h = R_s[1 - \sqrt{1 - (r_o/R_s)^2}]$, where r_i and r_o are the radii of circles on which the convex and concave vertices lie, respectively, and

Table 3
Comparison of elevations resulting from sharp and rounded polygonal cross sections with different material contact angles.

cos(θ)	Triangle		Rectangle		Pentagon		Hexagon	
	Sharp	R = 10 nm	Sharp	R = 10 nm	Sharp	R = 10 nm	Sharp	R = 10 nm
0.1	10.10	6.74	7.11	6.07	6.20	5.70	5.79	5.49
0.2	20.87	13.69	14.44	12.27	12.56	11.52	11.71	11.10
0.3	33.33	21.10	22.26	18.79	19.22	17.59	17.87	16.92
0.4	49.99	29.31	31.00	25.82	26.45	24.07	24.48	23.11
0.5		38.96	41.42	33.71	34.60	31.23	31.78	29.88
0.6		51.32	55.48	43.06	44.39	39.45	40.25	37.57
0.7		70.27	86.58	55.23	57.63	49.63	50.86	46.82
0.8				74.58	86.07	63.95	66.79	59.20
0.9						95.74		81.50

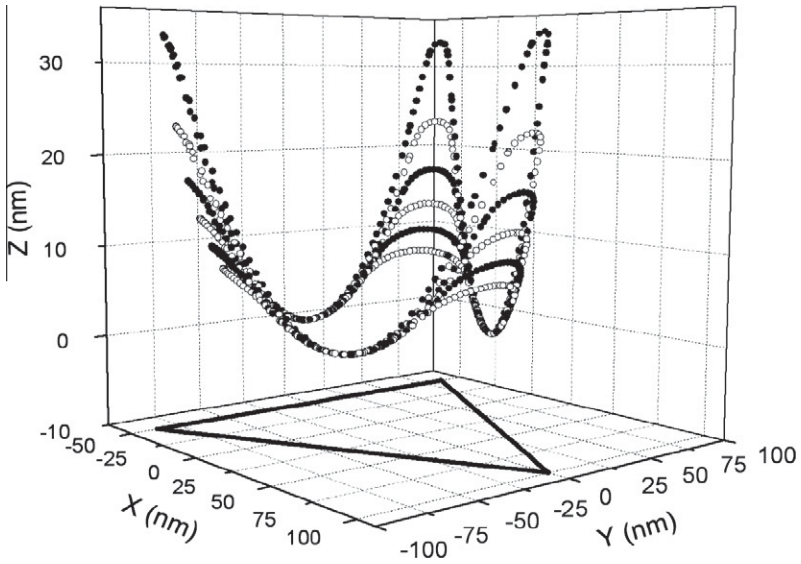

Fig. 5. 3D scatter plot of equilibrium contact lines resulting from capillaries with rounded triangular cross sections, rounding radius, R, from 0.05 to 0.30 with 0.05 increments top to bottom. The triangular frame which shared by all cross-sectional rounded triangles is also shown at the bottom. Notice that the Z coordinate is stretched compared to X and Y coordinates to accentuate the deformation of the meniscus.

n is the order of symmetry. The effective contact angle, in this case, can be determined by $\cos\theta_{eff} = l\ \cos\theta/[r_i \sin(\pi/n)]$, where $l = \sqrt{r_o^2 + r_i^2 - 2r_o r_i \cos(\pi/n)}$, then similarly, $h = r_o[1 - \sqrt{1 - (\cos\theta_{eff})^2}]/\cos\theta_{eff}$. Thus, as can be shown for polygons, changing the cross-sectional geometry of a capillary from a circle to a regular star effectively only changes the radius of the sphere on which the meniscus lies. In terms of elevation, it is equivalent to rescaling the cosine of contact angle, and the scaling factor is determined by the cross-sectional geometry. The critical contact angle becomes $\theta_c = \cos^{-1}[r_i \sin(\pi/n)/\sqrt{r_o^2 + r_i^2 - 2r_o r_i \cos(\pi/n)}]$ and is tabulated for various three-armed and four-armed stars in Table 4.

The simulation results of meniscus elevation, h, for a series of three-armed stars where the radius of the inscribed circle, r_i, was varied from 20 nm to 45 nm, while keeping the radius of the circumscribed circle r_o = 100 nm, are presented in Fig. 6a as a function of contact angle. For comparison, the predictions of theory are superimposed over the simulation data. The simulation results agree very well with the analytical solution. The error of any individual data point is found to be less than 1%. The same level of accuracy is observed with results of four-armed star cross sections as well. As seen in Fig. 6b, after rescaling the contact angles into effective contact angles, all data points of three-armed and four-armed star cross sections collapse on the theoretical curve of cylindrical capillary just as expected.

3.4. Rounded regular stars

As mentioned before, some degree of corner rounding is generally inevitable for the nanoscale features on the mold used in CFL experiments. On the other hand, star-shaped cross-sectional geometries provide appreciable capability of producing large elevations at relatively large contact angles. It is useful to find out whether

Table 4
Cosine and angular values of critical contact angle for regular stars.

	10 nm	20 nm	30 nm	40 nm	50 nm	60 nm	70 nm
Three-armed stars	0.091 85°	0.189 79°	0.292 73°	0.397 67°	0.500 60°		
Four-armed stars	0.076 86°	0.163 81°	0.260 75°	0.367 68°	0.480 61°	0.593 54°	0.700 46°

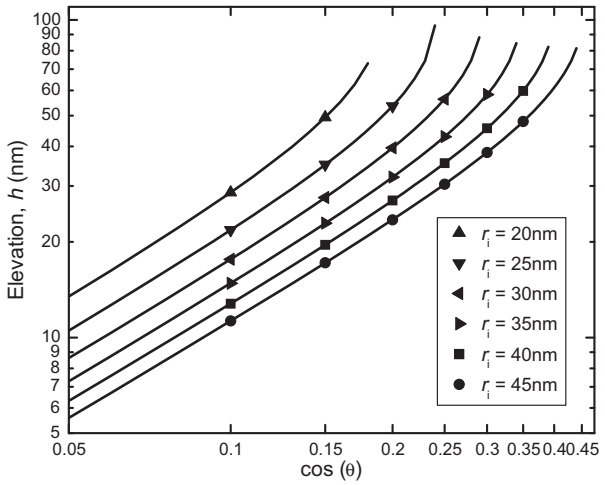

Fig. 6a. Elevation as a function of cosine of contact angle for three-armed stars with sharp corners. Data points represented by different symbols correspond to simulation results with different r_i values, while keeping r_o to be 100 nm. Solid lines are based on analytical solutions for respective cases.

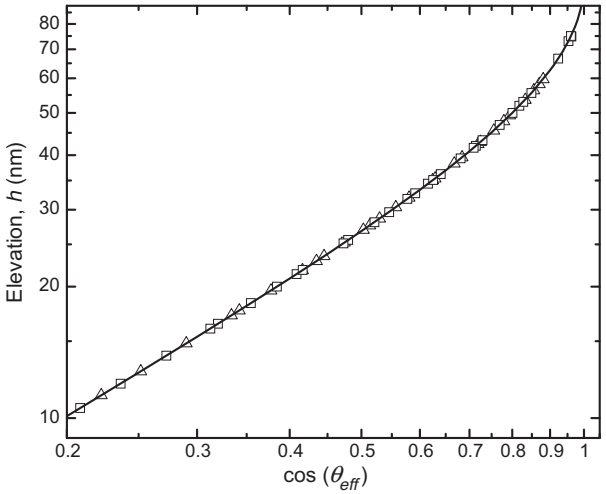

Fig. 6b. Elevation as a function of cosine of effective contact angle for three-armed stars (hollow triangles) and four-armed stars (hollow squares) with sharp corners on a log–log scale. All the data points collapse on the analytical solution for circular cross section (solid line) as expected.

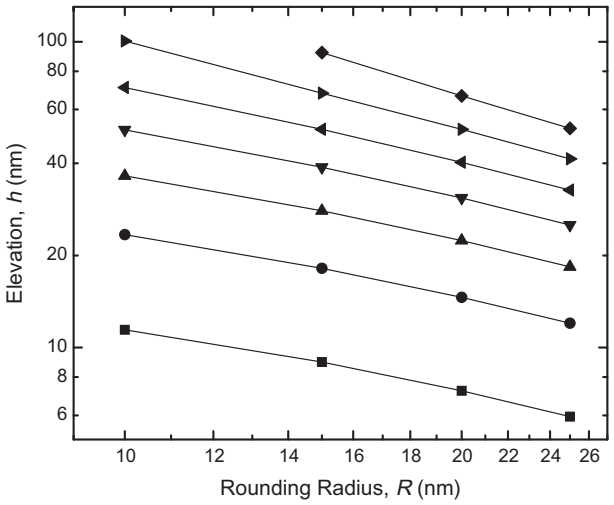

Fig. 7. Elevation as a function of rounding radius for three-armed stars with the same outer frame (r_o = 1.5, r_i = 0.5). Each curve represents a different value of cos(θ), including: (■) 0.1, (●) 0.2, (▲) 0.3, (▼) 0.4, (◄) 0.5, (►) 0.6, and (♦) 0.7, from bottom to top.

the star-shaped geometry can offer significant elevation improvement in the cases where corners are rounded. Therefore, simulations were performed to study the effects of corner rounding to regular star cross-sectional geometry. Similar to what was observed in the polygon cases, when the convex corners of a star-shape are rounded, the elevation achieved at the point of each arm of the star decreases with increasing degrees of rounding. As mentioned before, this reduction in elevation is the combined result of two effects – slight decrease in length scale and reducing of confinement at the corners due to rounding. The overall response to corner rounding of a three-armed star is plotted in Fig. 7. Similar results were achieved for the four-armed stars. For cases where rounding radius is moderate, the elevation has a power law dependence on rounding radius. The power law exponent is found to become more strongly negative with decreasing contact angle, ranging from −0.7 at cos(θ) = 0.1 to −1.1 at cos(θ) = 0.7. These slopes are tabulated in Table 5.

Considering the sum total of these simulations allows us to focus on some very interesting questions. For instance, what should one do if one wants to fabricate a novel and useful three-dimensional nanostructure that has tunable rotational symmetry and large height variation utilizing capillary effects in lithography? Both polygons and stars will work. However, the star is clearly the optimal geometry. Even when the corners are inevitably rounded due to the limitation of fabrication tools, high elevations can still be achieved owing to the large confinement effects. Let's take a close look at Fig. 7 and the elevations corresponding to different rounding radius for a certain set of three-armed stars with r_o = 150 nm and r_i = 50 nm. Notice that for a fluid–solid pair with contact angle of about 53° and a corner rounding of 20 nm in diameter, an elevation of approximately h = 116 nm can be achieved along the meniscus. For comparison, a triangular cross section with the same characteristic dimension and corner rounding and same contact angle would result in an elevation of only 77 nm. These two surfaces are presented in Fig. 8a for comparison. This represents just one example of nanoscale claw-like structure that can be formed. If one wants to push the limit to maximize elevation, one could simply choose geometries with higher r_o/r_i ratios, so that the internal corners of the convex vertex of the star-shape gets sharper or minimize the corner rounding. Moreover, since confinement factor is independent of symmetry order, one can make nano-claws with arbitrary number of fingers (Fig. 8b) without having to sacrifice elevation. Specifically, for a regular polygon the internal angle is directly related to the number of sides, and the elevation on the meniscus, h, decreases significantly with the increase of number of sides, n, when n ranges from 3 to 6. For a regular star, on the other hand, the internal angle at the convex corners is mostly dependent on the r_o/r_i ratio and is rather insensitive to the order of symmetry. Clearly, the elevation difference between the four-armed star and the rectangle geometries shown in Fig. 8b is much more significant than the elevation difference between the three-armed star and the triangle geometries shown in Fig. 8a.

4. Conclusion

In the work described within this paper, simulation results were presented which demonstrated that high aspect ratio three-dimensional nanostructures can be achieved by CFL with proper choice of cross-section geometries. A series of regular polygons and star-shapes with both sharp and rounded corners were studied. For

Table 5
Slopes of the elevation (h) versus rounding radius (R) log–log curves for rounded three-armed star cross sections.

$\cos(\theta)$	0.1	0.2	0.3	0.4	0.5	0.6	0.7
Triangles	−0.288	−0.293	−0.300	−0.312	−0.333	−0.369	−0.444
Three-armed stars	−0.711	−0.722	−0.743	−0.779	−0.841	−0.965	−1.116

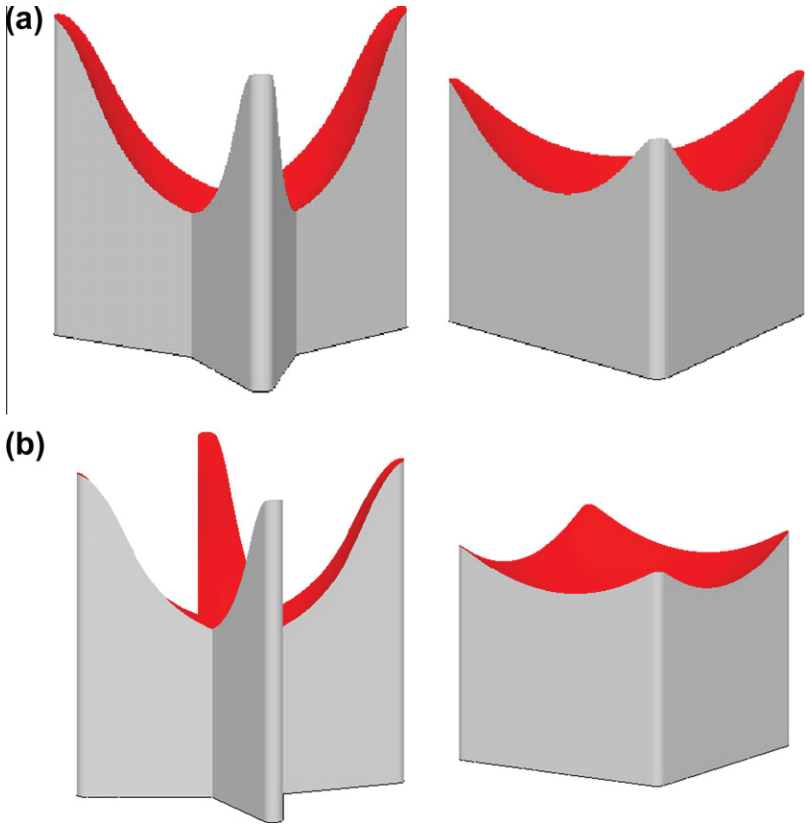

Fig. 8. Comparison of the meniscus shapes for: (a) three-armed star cross section (r_o = 150 nm, r_i = 50 nm, R = 10 nm, $\cos(\theta)$ = 0.6) and triangular cross section (r = 150 nm, R = 10 nm, $\cos(\theta)$ = 0.6) with the same vertices; and (b) four-armed star cross section (r_o = 200 nm, r_i = 50 nm, R = 10 nm, $\cos(\theta)$ = 0.55) compared with rectangular cross section (r = 200 nm, R = 10 nm, $\cos(\theta)$ = 0.55) with the same vertices.

sharp corner polygons and stars, the simulation results were shown to match the analytical solutions for elevation of the meniscus, demonstrating the accuracy of the simulations. It was shown that, as far as the elevation and the shape of the meniscus are concerned, altering the cross-sectional geometry from a circle to a regular polygon or to a regular star is effectively equivalent to simply changing the contact angle between the fluid and the capillary wall. Numerical solutions for elevation of the meniscus formed in rounded corner polygons and stars cross sections were calculated based on simulation results. The rounding of corners not only reduced elevation but also modified the shape of the meniscus. At a given contact angle, elevation decreased as rounding radius increased, following clear power laws within the regime of rounding radius between 10 nm and 30 nm. The specific power index, which ranged from −0.3 to −1.1, varied with geometry, contact angle, and degree of corner rounding. The sharp-corner cases are good starting point for understanding the effects of different parameters on the equilibrium meniscus, while the rounded-corner cases capture a rather important practical aspect in CFL experiments; namely the inability to fabricate perfectly sharp corners at the nanometer length scales. It is shown in this study that even with moderate corner rounding, large elevations on the meniscus can still be achieved especially when using star-shaped capillaries.

Acknowledgments

The authors would like to thank Professor Mark T. Tuominen for helpful discussions and Craig W. Versek for very useful assistance with Python coding. This work was supported by NSF Center for Hierarchical Manufacturing at UMASS under Grant number CMMI-0531171.

References

[1] Kahp Y. Suh, Yun S. Kim, Hong H. Lee, Adv. Mater. 13 (18) (2001) 1386–1389.
[2] Kahp Y. Sch, Hong H. Lee, Adv. Funct. Mater. 12 (2002) 405–413.
[3] Christiaan M. Bruinink, Mária Péter, Meint de Boer, Laurens Kuipers, Jurriaan Huskens, David N. Reinhoudt, Adv. Mater. 16 (13) (2004) 1086–1090.
[4] Christiaan M. Bruinink, Mária Péter, Pascale A. Maury, Meint de Boer, Laurens Kuipers, Jurriaan Huskens, David N. Reinhoudt, Adv. Funct. Mater. 16 (2006) 1555–1565.
[5] Jin-Mi Jung, Francesco Stellacci, Hee-Tae Jung, Adv. Mater. 19 (2007) 4392–4398.
[6] Su Yeon Lee, Jong-Ryul Jeong, Shin-Hyun Kim, Sarah Kim, Seung-Man Yang, Langmuir 25 (21) (2009) 12535–12540.
[7] Sung-Hoon Lee, Hong-Nam Kim, Rho-Kyun Kwak, Kahp Y. Suh, Langmuir 25 (20) (2009) 12024–12029.
[8] Kahp-Yang Suh, Min Cheol Park, Pilnam Kim, Adv. Funct. Mater. (19) (2009) 2699–2712.
[9] Robert Finn, Equilibrium Capillary Surfaces, Springer-Verlag, 1986, ISBN 0-387-96174-7 (Chapter 6).
[10] G. Smedley, Microgravity Sci. Technol. 3 (1) (1990) 13–23.

[11] P. Concus, R. Finn, Microgravity Sci. Technol. 3 (2) (1990) 87–92.
[12] Harris Wong, S. Morris, C.J. Radke, J. Colloid Interface Sci. 148 (1992) 317–336.
[13] H.D. Mittelmann, A. Zhu, Microgravity Sci. Technol. 9 (1) (1996) 22–27.
[14] Steven H. Collicott, Mark M. Weislogel, AIAA J 42 (2) (2004) 289–295.
[15] Kahp Y. Suh, Pilnam Kim, Hong H. Lee, Appl. Phys. Lett. 85 (18) (2004) 4019–4020.
[16] Kenneth A. Brakke, Exp. Math. 1 (1992) 141–165.
[17] P.G. de Gennes, Rev. Mod. Phys. 57 (1985) 827–863.
[18] Pierre-Gilles de Gennes et al., Capillarity and Wetting Phenomena – Drops, Bubbles, Pearls, Waves, Springer, 2004, ISBN 0-387-00592-7 (Chapter 2).
[20] Paul Concus, Robert Finn, Acta Math. 132 (1974) 177–198.
[21] Robert Finn, Not. AMS 46 (7) (1999) 770–781.